ADVANCED PHYSICS RESEARCH Open Access
www.advphysicsres.com

Ferroelectric Control of Anisotropic Magnetoresistance in Ultrathin Sr_2IrO_4 Films toward 2D Metallic Limit

*Yuanyuan Zhang, Qiuchen Wu, Yifei Hao, and Xia Hong**

The Ruddlesden-Popper 5*d* iridate Sr_2IrO_4 is an antiferromagnetic Mott insulator with the electronic, magnetic, and structural properties highly intertwined. Voltage control of its magnetic state is of intense fundmenatal and technological interest but remains to be demonstrated. Here, the tuning of magnetotransport properties in 5.2 nm Sr_2IrO_4 via interfacial ferroelectric $PbZr_{0.2}Ti_{0.8}O_3$ is reported. The conductance of the epitaxial $PbZr_{0.2}Ti_{0.8}O_3/Sr_2IrO_4$ heterostructure exhibits ln(*T*) behavior that is characteristic of 2D correlated metal, in sharp contrast to the thermally activated behavior followed by 3D variable range hopping observed in single-layer Sr_2IrO_4 films. Switching $PbZr_{0.2}Ti_{0.8}O_3$ polarization induces nonvolatile, reversible resistance modulation in Sr_2IrO_4. At low temperatures, the in-plane magnetoresisance in the heterostructure transitions from positive to negative at high magnetic fields, opposite to the field dependence in single-layer Sr_2IrO_4. In the polarization down state, the out-of-plane anisotropic magnetoresistance R_{AMR} exhibits sinusoidal angular dependence, with a 90° phase shift below 20 K. For the polarization up state, unusual multi-level resistance pinning appears in R_{AMR} below 30 K, pointing to enhanced magnetocrystalline anisotropy. The work sheds new light on the intriguing interplay of interface lattice coupling, charge doping, magnetoelastic effect, and possible incipient ferromagnetism in Sr_2IrO_4, facilitating the functional design of its electronic and material properties.

1. Introduction

The Ruddlesden-Popper series of 5*d* iridates $Sr_{n+1}Ir_nO_{3n+1}$ ($n = 1, 2, \ldots, \infty$) represents a model system where the electronic and magnetic states can by systematically tuned by the competition between spin-orbit coupling (SOC) and onsite Coulomb energy.[1] With the bandwidth increasing with n, $Sr_{n+1}Ir_nO_{3n+1}$ varies from a Mott insulator to a correlated semimetal.[2] As an end member of the series, Sr_2IrO_4 (SIO, $n = 1$) is a $J_{eff} = 1/2$ antiferromagnetic Mott insulator.[1,3] The strong SOC and Dzyaloshinskii-Moriya interaction induce spin canting, resulting in weak net moments and pronounced magnetic anisotropy.[1] Due to the close interplay between the charge, spin, orbital, and lattice degrees of freedom, various control knobs can be exploited to design the functionalities of this material. For example, high electrical current can induce lattice expansion and an incipient metallic state in bulk Sr_2IrO_4.[4] In epitaxial thin films, the substrate strain can effectively modulate the electronic correlation energy,[5] modify the magnetocrystalline anisotropy (MCA),[6] and tune the magnetic order and in-plane net magnetization.[7] Large orthorhombic distortion imposed in $Sr_2IrO_4/Ca_3Ru_2O_7$ heterostructures also leads to inverted interlayer exchange coupling.[8]

Among various control mechanisms, the carrier density directly modifies the Coulomb energy in correlated oxides, which promises charge induced metal-insulator transitions and modification of the magnetic states.[9] Due to the structural and magnetic similarities between Sr_2IrO_4 and La_2CuO_4,[8] whether doping can introduce superconductivity in Sr_2IrO_4 also remains an intriguing question.[10] In previous studies, doping control in Sr_2IrO_4 has been achieved via chemical substitution,[11–15] interface charge transfer with other correlated oxides,[16] and ionic liquid gating.[17,18] While metal-insulator transitions have been observed in $(Sr,La)_2IrO_4$[12] and $Sr_2(Ir,Rh)O_4$,[13,15] chemical doping concomitantly modifies the lattice distortion, complicating the dominating physical mechanism. Also, for the chemical doping and interface charge transfer approaches, the doping level is not tunable. The ionic liquid gating has led to substantial tuning of the carrier density in Sr_2IrO_4 thin films, yielding large modulation of conduction.[17,18] However, the presence of high density surface ions can induce oxidation or reduction of the material, change the surface chemistry, and create defect states, which can irreversibly deteriorate the sample quality.[19]

Y. Zhang, Q. Wu, Y. Hao, X. Hong
Department of Physics and Astronomy
University of Nebraska-Lincoln
Lincoln, Nebraska 68588-0299, USA
E-mail: xia.hong@unl.edu
X. Hong
Nebraska Center for Materials and Nanoscience
University of Nebraska-Lincoln
Lincoln, Nebraska 68588-0298, USA

The ORCID identification number(s) for the author(s) of this article can be found under https://doi.org/10.1002/apxr.202400208

DOI: 10.1002/apxr.202400208

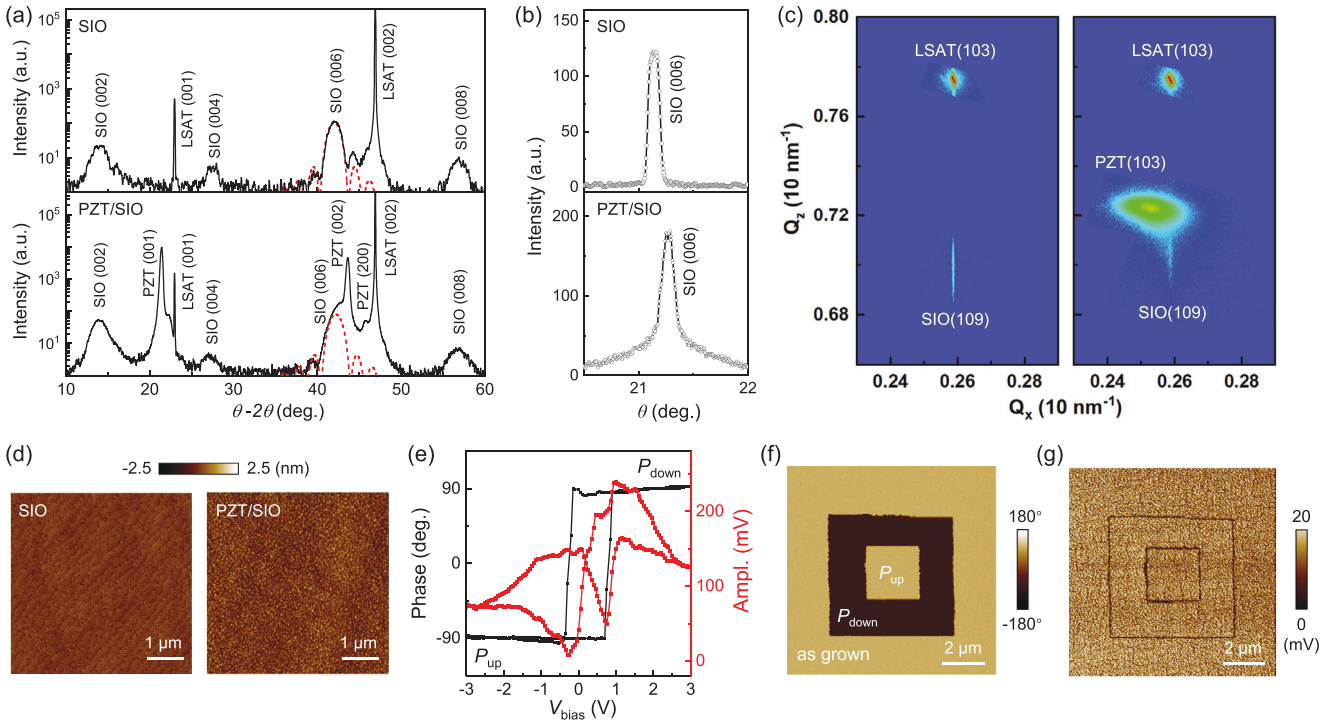

Figure 1. Characterization of a 5.2 nm Sr_2IrO_4 film and a 150 nm PZT/5.2 nm Sr_2IrO_4 heterostructure grown on (001) LSAT substrate. a) XRD θ -2θ scans with fits to the Laue oscillations of the SIO (006) peak (dotted line) for the single-layer Sr_2IrO_4 (top) and PZT/Sr_2IrO_4 heterostructure (bottom). b) Rocking curves of Sr_2IrO_4 (006) peak for the single-layer (top) and heterostructure (bottom) samples. c) Reciprocal space maps of single-layer Sr_2IrO_4 (left) and PZT/Sr_2IrO_4 heterostructure (right) around the (103) peak of LSAT. d) AFM topography images of single-layer Sr_2IrO_4 (left) and PZT/Sr_2IrO_4 heterostructure (right). e-g) PFM studies of a PZT/Sr_2IrO_4 heterostructure. e) PFM phase and amplitude switching hysteresis. f) PFM phase and g) amplitude images of concentric square domains written on the sample.

A powerful approach to induce reversible and nonvolatile modulation of the carrier density is the ferroelectric field effect.[9] Ferroelectric perovskite oxides such as $Pb(Zr,Ti)O_3$ can be interfaced with Sr_2IrO_4 in the epitaxial heterostructure form. The large polarization field P promises a 2D carrier density modulation of $2P \sim 10^{15}$ cm^{-2},[20] comparable with the intrinsic doping level of Sr_2IrO_4 thin films.[18] In previous studies, the ferroelectric field effect has been applied to various correlated oxides, e.g., modulating metallicity in $RNiO_3$ (R = rare earth),[20,21] $(La,Sr)MnO_3$,[22] and VO_2,[23] tuning superconductivity in cuprates,[24,25] controlling magnetic order[26,27] and magnetic anisotropy[28–31] in $(La,Sr)MnO_3$, and inducing emergent antiferromagnetic order in EuO.[32] It also enables the functional design of various energy-efficient nanodevices[33,34] such as ferroelectric-gated Mott transistors[20,35] and ferroelectric tunnel junctions.[36–39]

In this work, we report the nonvolatile ferroelectric control of the metallicity and magnetotransport properties of ultrathin Sr_2IrO_4 films interfaced with $PbZr_{0.2}Ti_{0.8}O_3$ (PZT). While the single-layer Sr_2IrO_4 film exhibits thermally activated behavior followed by 3D variable range hopping (VRH) transport, the epitaxial PZT/Sr_2IrO_4 heterostructure shows 2D correlated conduction. Switching the polarization of PZT leads to reversible, nonvolatile modulation of resistance and magnetoresistance (MR) in Sr_2IrO_4. At low temperatures, the in-plane MR of the heterostructure transitions from positive to negative with increasing magnetic field, opposite to the field dependence in single-layer Sr_2IrO_4, which has been attributed to the emergence of an incipient ferromagnetic state with the transition temperature close to 6 K. The out-of-plane anisotropic magnetoresistance (AMR) in the polarization down (P_{down}) state exhibits sinusoidal angular dependence, with a 90° phase shift at low temperatures. Unusual multi-level resistance pinning emerges in the polarization up (P_{up}) state, indicating enhanced magnetocrystalline anisotropy. Our study reveals the complex interplay of interfacial lattice coupling, charge doping, magnetoelastic effect, and possible incipient ferromagnetism in Sr_2IrO_4, providing important material information for designing its electronic and material properties.

2. Results and Discussion

We deposit epitaxial 150 nm PZT/5.2 nm Sr_2IrO_4 heterostructures and single-layer 5.2 nm Sr_2IrO_4 films on (001) $(LaAlO_3)_{0.3}(Sr_2AlTaO_6)_{0.7}$ (LSAT) substrates using off-axis radio frequency magnetron sputtering (see experimental section for detailed growth conditions). X-ray diffraction (XRD) measurements reveal (001) growth for PZT and Sr_2IrO_4 layers with no apparent impurity phases (**Figure 1a**). The full-width-half-maximum of the rocking curves for the Sr_2IrO_4 (006) peak is 0.11° for the single-layer film and 0.16° for the heterostructure (Figure 1b). The narrow peaks indicate high crystallinity of the samples. The growth rate is calibrated using Laue oscillation around the (006) Bragg peak (Figure 1a) and x-ray reflectivity measurements (Figure S1, Supporting Information). Figure 1c

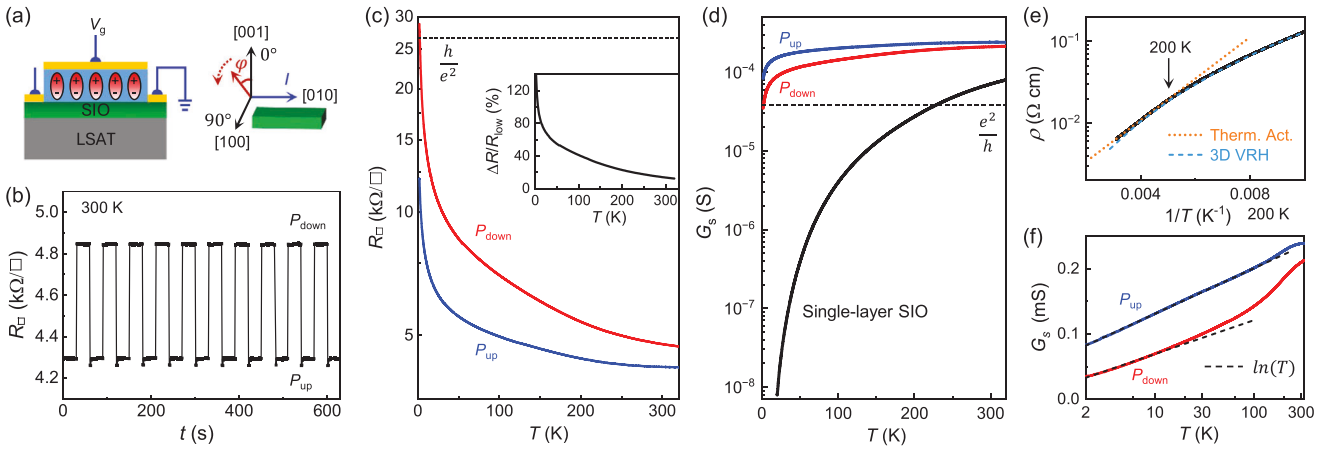

Figure 2. Transport properties of single-layer Sr_2IrO_4 and PZT/Sr_2IrO_4 heterostructure. a) Schematic experimental setup. b) $R_\square$ switching upon application of $V_g = \pm 3$ V voltage pulses. c) $R_\square$ versus T for both polarization states of PZT/Sr_2IrO_4. Inset: $\Delta R/R_{low}$ versus T. d) G_s versus T for single-layer Sr_2IrO_4 and P_{down} and P_{up} states of PZT/Sr_2IrO_4 heterostructure. e) Arrhenius plot of ρ versus $1/T$ for single-layer Sr_2IrO_4 with fits to thermally activated behavior (dotted line) and 3D VRH (dashed line). f) Linear-log plot of G_s versus T for PZT/Sr_2IrO_4 heterostructure in both polarization states with fits to Equation 1 (dashed lines).

shows the reciprocal space mapping around the (103) Bragg peak of LSAT. Both the single-layer Sr_2IrO_4 and the Sr_2IrO_4 layer in the heterostructure are fully strained to the substrates, with the in-plane lattice constant $a_0 = 3.865$ Å. The c-axis lattice constant is $c_0 = 12.885$ Å for single-layer Sr_2IrO_4 and $c_0 = 12.772$ Å for Sr_2IrO_4 in the heterostructure, with the bulk unit cell of $\sqrt{2}a_0 \times \sqrt{2}a_0 \times 2c_0$. Atomic force microscopy (AFM) characterizations reveal smooth surface morphology for single-layer Sr_2IrO_4 and PZT/Sr_2IrO_4 heterostructures (Figure 1d), with typical root-mean-square surface roughness of ~2 Å and ~4 Å, respectively. Piezoresponse force microscopy (PFM) studies show robust switching hysteresis in PZT/Sr_2IrO_4 at room temperature, with coercive voltages of −0.3 V (0.8 V) for the P_{up} (P_{down}) state (Figure 1e). Figure 1f,g shows the PFM phase and amplitude images, respectively, of concentric square domains written on a PZT/Sr_2IrO_4 heterostructure. In the as-grown state, the PZT layer is uniformly polarized in the P_{up} state, which is consistent with the lower coercive field (Figure 1e).

The PZT/Sr_2IrO_4 heterostructures are fabricated into field effect transistor devices, with the Sr_2IrO_4 channel patterned into a Hall bar geometry. The details of the device fabrication can be found in Ref. [20]. The current channel is along [010] direction, with the channel length of 10–80 μm and length/width aspect ratio of 2. For the MR measurements, the magnetic field lies in the plane perpendicular to the current direction (**Figure 2a**). Figure 2b shows the sheet resistance ($R_\square$) at 300 K of a heterostructure sample upon a series of gate voltage (V_g) pulses with alternating signs (±3 V) applied to PZT. The P_{up} (P_{down}) state corresponds to hole accumulation (depletion), resulting in lower (higher) channel resistance R_{low} (R_{high}). This is consistent with the p-type doping of single-layer Sr_2IrO_4,[18,40] as confirmed by Hall measurements (Section S3, Supporting Information). The resistance switching is nonvolatile and fully reversible, with no appreciable decay observed after removal of V_g for both polarization states. The resistance switching ratio $\Delta R/R_{low} = (R_{high}-R_{low})/R_{low}$ is 13% at 300 K.

Figure 2c shows $R_\square(T)$ of a PZT/Sr_2IrO_4 heterostructure in the P_{up} and P_{down} states of PZT. To ensure full polarization reversal, we apply $V_g = \pm 3$ V to the heterostructure at 300 K, well exceeding the coercive voltages (Figure 1e). The negligibly small relaxation in both resistance states (Figure 2b) suggests low density charge trapping states, e.g., oxygen vacancies, at the PZT/Sr_2IrO_4 interface.[41] The $\Delta R/R_{low}$ increases monotonically with decreasing temperature, reaching 139% at 2 K (Figure 2c inset). Surprisingly, the heterostructure is significantly more conductive than the single-layer sample in both polarization states, with the conductance enhanced by more than four orders of magnitude at 20 K (Figure 2d). For single-layer Sr_2IrO_4, the resistivity ρ above 200 K can be well described by the thermally activated behavior, $\rho \propto \exp(\frac{\Delta}{2k_BT})$ (Figure 2e). The extracted activation energy gap Δ is 100 meV, similar to previously reported values for Sr_2IrO_4 single crystals[12] and thin films.[42] Below 200 K, $\rho(T)$ follows the 3D variable range hopping behavior,[43] $\rho \propto \exp(\frac{T_0}{T})^{\frac{1}{4}}$ with T_0 the characteristic temperature (Section S3, Supporting Information), suggesting that the system is strongly localized. In sharp contrast, the conductance of the heterostructure exhibits ln(T) behavior at low temperatures (Figure 2f), which signals a 2D weakly localized metal. This is consistent with the fact that $R_\square$ in the heterostructure is below the 2D quantum resistance limit of $h/e^2 \approx 25.8$ kΩ at this temperature range. Since the system is close to the boundary between the weakly localized and strongly localized regimes,[44] the ln(T) behavior persists to very high temperature (e.g., ~100 K for the P_{up} state), and we do not observe a crossover to positive dR/dT up to 320 K. Fitting the temperature dependence of sheet conductance G_s to:[45]

$$G_s(T) = G_0 + p\frac{e^2}{2\pi^2\hbar}\ln\left(\frac{T}{T_0'}\right) \quad (1)$$

where G_0 is the Drude conductance, e is the electron charge, $\hbar$ is the reduced Planck constant, and p and T_0' are fitting parameters, we deduce $p = 1.8$ for the P_{down} state and $p = 2.5$ for the

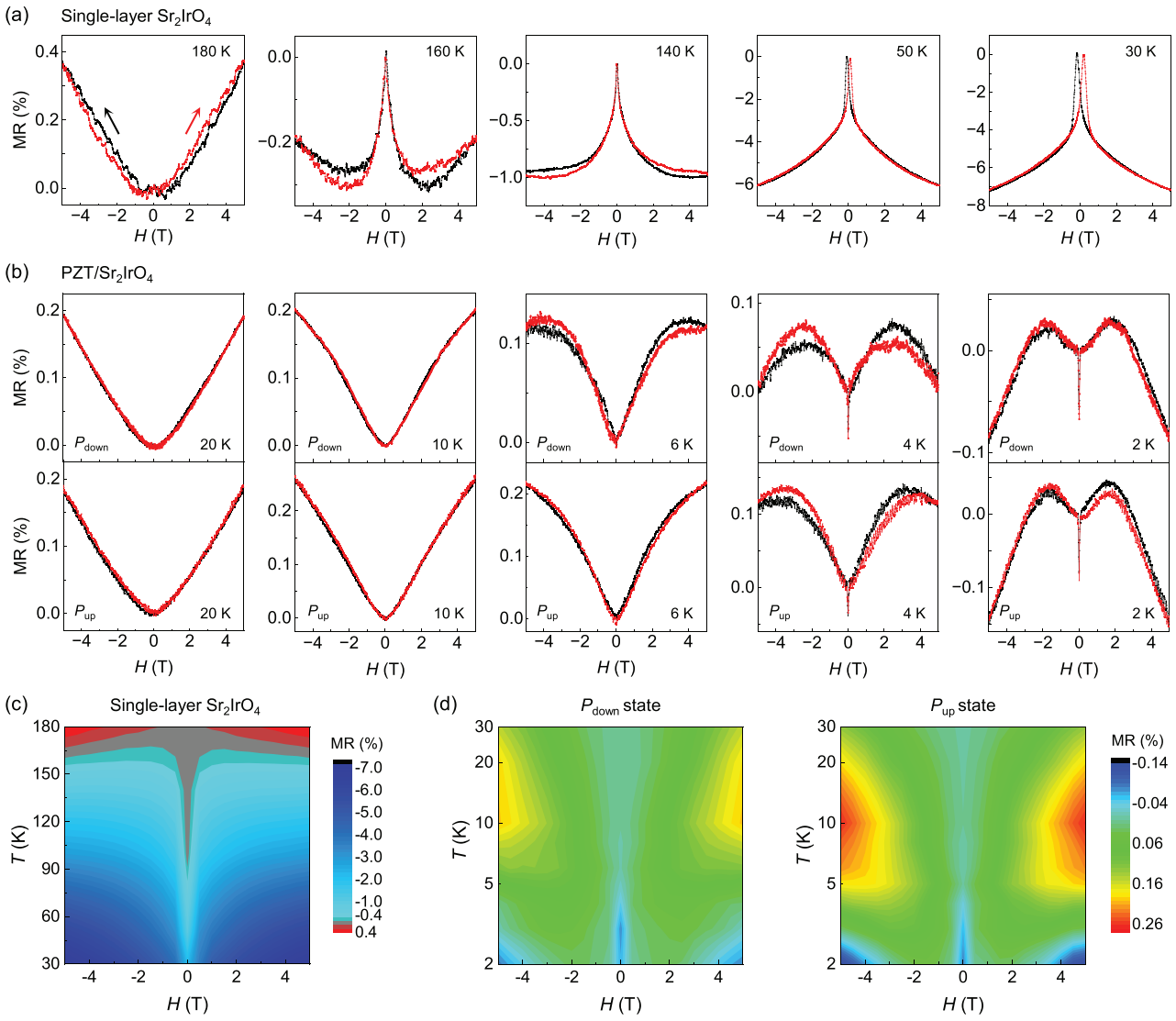

Figure 3. In-plane MR as a function of temperature and magnetic field. a) In-plane MR for single-layer Sr_2IrO_4. The red (black) curves correspond to the upward (downward) sweep of H. b) In-plane MR for the P_{down} (top) and P_{up} (bottom) states of PZT/Sr_2IrO_4. The sweep rate for H is 100 Oe/s. c,d) Contour plots of MR versus H and T for the up sweep of H. c) Single-layer Sr_2IrO_4. d) P_{down} (left) and P_{up} (right) states of PZT/Sr_2IrO_4.

P_{up} state, pointing to a 2D metallic system subjected to the convoluted effects of electron-electron ($p = 1$) and electron-phonon ($p = 3$) interactions.[46,47] This result suggests that the presence of PZT has modified the electronic state in interfacial Sr_2IrO_4, inducing not only a metal-insulator transition but also a dimensionality crossover from 3D to 2D. The metallic state is also consistent with the smaller unit cell volume for the heterostructure sample (Figure 1c).

It is important to note that the 2D metallic state in the heterostructure sample is not induced by the polarization doping. For both polarization states, the 3D resistivity of the heterostructure ranges from 10^{-3} to 10^{-2} Ω cm, close to that of chemically doped Sr_2IrO_4 that exhibits a metal-insulator transition.[11–13,15] One possible mechanism that contributes to the metal-insulator transition is the chemical pressure induced by interfacial atomic bonding with PZT. Previous studies of electrical current induced metallic state in bulk Sr_2IrO_4 have shown that the metallic state is accompanied with the reduced oxygen octahedral rotation in the basal plane.[4] As the in-plane octahedral rotation is relatively small for PZT (tolerance factor of 1.008),[48] it is conceivable that bonding with PZT would straighten the Ir—O—Ir bond angle in interfacial Sr_2IrO_4 and hence increase its electronic bandwidth.

Next, we investigate the effect of the interfacial ferroelectric layer on the in-plane magnetoresistance (MR = $[R(H)-R(0)]/R(0)$) of Sr_2IrO_4. **Figure 3a** shows the in-plane MR for the single-layer Sr_2IrO_4 as a function of magnetic field H (parallel to the [100] direction) at various temperatures. At 180 K, the sample exhibits positive, parabolic field dependence with noticeable hysteresis at high magnetic fields, which can be attributed to the magnetoelastic effect.[18] As the temperature decreases to 160 K, negative MR emerges at low magnetic fields and transitions to positive MR above 2 T. Below 140 K, negative MR dominates

the entire magnetic field range up to 5 T. A clear hysteresis at low magnetic field emerges at 50 K. The hysteresis window increases with decreasing temperature, with MR peaking at +0.2 T (-0.2 T) for the upward (downward) field sweep. The temperature and magnetic field dependences of in-plane MR are consistent with previous reports for Sr_2IrO_4 thin films.[18,49] The low-field hysteresis has been attributed to the spin-flip transition in the antiferromagnetic state, leading to the aligned in-plane magnetic moment between adjacent basal planes.[50,51] It also explains the substantial increase of negative MR with decreasing temperature, which corresponds to suppressed spin scattering in a higher magnetic field.

The difference in the electronic state between the single-layer Sr_2IrO_4 film and PZT/Sr_2IrO_4 heterostructure is also manifested in the distinct MR behaviors. For the heterostructure sample, the positive MR with parabolic field dependence persists down to 20 K with negligble hysteresis (Figure 3b and Figure S5, Supporting Information). In the P_{down} state, as the temperature decreases to 10 K, the MR exhibits a transition from concave to convex shape at ~3 T, while at 6 K, the negative MR emerges at 4 T, which is accompanied by a clear hysteresis. The negative MR component increases progressively with decreasing temperature. At 4 K, the positive and negative contributions fully cancel each other at 5 T, and the negative MR dominates at high field at 2 K. In the P_{up} state, the sample exhibits qualitatively similar temperature and magnetic field dependences of the MR, while the transition from positive MR to negative MR occurs at lower temperatures and higher magnetic fields (Figure 3b). At 10 K, the transition from concave to convex shape occurs at ~5 T, leading to a higher positive MR at 5 T in P_{up} state (0.26%) compared to that in P_{down} state (0.20%). The magnitude and magnetic field dependence of MR at 4 K in the P_{up} state closely resemble that of the P_{down} state at 6 K. On the other hand, the negative MR in the P_{up} state increases more rapidly with decreasing temperature. At 2 K, the negative MR at 5 T reaches −0.15% for the P_{up} state and −0.08% for the P_{down} state.

The distinct temperature and magnetic field dependences of MR are illustrated in the contour plots of MR for the single-layer Sr_2IrO_4 (Figure 3c) and PZT/Sr_2IrO_4 heterostructure (Figure 3d). The single-layer Sr_2IrO_4 film displays comparable positive MR values to the heterostructure sample but significantly higher negative MR magnitudes. Its positive-to-negative MR transition occurs at a much higher temperature, ~160 K, and at lower fields. For the heterostructure sample, the P_{down} and P_{up} states exhibit qualitatively similar temperature and magnetic field dependences of MR, despite the modulation of critical temperature/magnetic field for the positive-to-negative MR transition.

The evolution of MR indicates the competition of two mechanisms with different temperature dependences: the positive MR is due to the magnetoelastic effect, which can also contribute to the high field hysteresis;[18] the negative MR can be attributed to the suppressed spin scattering in a magnetic field. Compared with the single-layer Sr_2IrO_4, the negative MR in the heterostructure is significantly smaller (Figure 3c,d), and more importantly, the low-field hysteresis becomes absent. These observations collectively point to the change of magnetic state in the PZT/Sr_2IrO_4 heterostructure. It is the presence of interfacial PZT alone, rather than the ferroelectric polarization of PZT, that induces substantial hole doping in Sr_2IrO_4, which fundamentally alters its metallicity and magnetic state. Indeed, Hall effect measurements show that the sheet carrier density in PZT/Sr_2IrO_4 can be more than one order of magnitude higher than single-layer Sr_2IrO_4, while switching the polarization only induces ~15% change of carrier density in the heterostructure (Section S3, Supporting Information).

A possible scenario for the distinct MR behavior is that the substantial hole doping drives the heterostructure sample close to the antiferromagnetic/ferromagnetic phase bounary, enabling a magnetic field induced incipient ferromagnetic state. In transition metal oxides, charge doping can facilitate the double-exchange mechanism and enable ferromagnetic coupling,[52] which competes with the superexchange induced antiferromagnetic order in single-layer Sr_2IrO_4. An emergent ferromagnetic state naturally explains three features of the in-plane MR: 1) the absence of low-field hysteresis; 2) the substantially smaller negative MR compared with the single-layer sample; and 3) the lower positive-to-negative MR transition temperature and larger low temperature negative MR in the P_{up} state (Figure 3). First, as the low-field hysteresis results from the spin-flip transition, it does not appear in the incipient ferromagnetic state. Second, the magnitude of negative MR reflects the relative change of spin scattering. For single-layer Sr_2IrO_4, the net moment results from spin canting, which is small and can change substantially in a magnetic field. In the ferromagnetic state, on the other hand, the spin orientation has already been aligned. At low temperature, the magnetic field induced moment change is relatively small compared to the net magnetization, rendering a small change in spin scattering and MR. Third, given that hole doping in Sr_2IrO_4 changes Ir^{4+} ($5d^5$) to Ir^{5+} ($5d^4$), we expect a smaller net magnetization in the P_{up} state. The relative change of net moment in magnetic field is thus higher compared with the P_{down} state, giving rise to the enhanced negative MR at low temperature. From the temperature dependence, we estimate the transition temperature for the incipient ferromagnetic state (T_{iFM}) to be close to while above 6 K, and it is higher in the P_{down} state.

Below T_{iFM}, another intriguing feature appears in the MR of the heterostructure. Sharp resistance dips emerge when the magnetic field sweeps across zero. The magnitude of resistance jump decreases with decreasing sweeping rate of H, and the dip disappears when the rate is reduced from 100 Oe/s to 25 Oe/s (Figure S6, Supporting Information). A plausible time-dependent mechanism is the slow structure change due to oxygen octahedral rotation. Due to the strong spin-orbital locking in Sr_2IrO_4,[53] the change in magnetic state is accompanied by substantial lattice change in the Ir—O—Ir bond angle, as demonstrated in chemically doped samples.[12] Assuming in equilibrium Sr_2IrO_4 is in the antiferromagnetic state and transitions to the ferromagnetic state in a magnetic field, it can transition from a highly distorted orthorhombic structure to a less distorted pseudo-tetragonal structure. Fast magnetic field sweep creates a transient lattice state with straightened Ir—O—Ir bonds at $H = 0$ T with large electronic bandwidth, leading to a sudden dip in resistivity. At slower sweeping rates, the system has sufficient time to relax into the highly distorted orthorhombic structure with large oxygen octahedral rotation, and the resistance dip diminishes.

We then investigate the out-of-plane AMR, with the magnetic field H rotating within the plane perpendicular to the current and making an angle φ with respect to the [001] direction (Figure 2a).

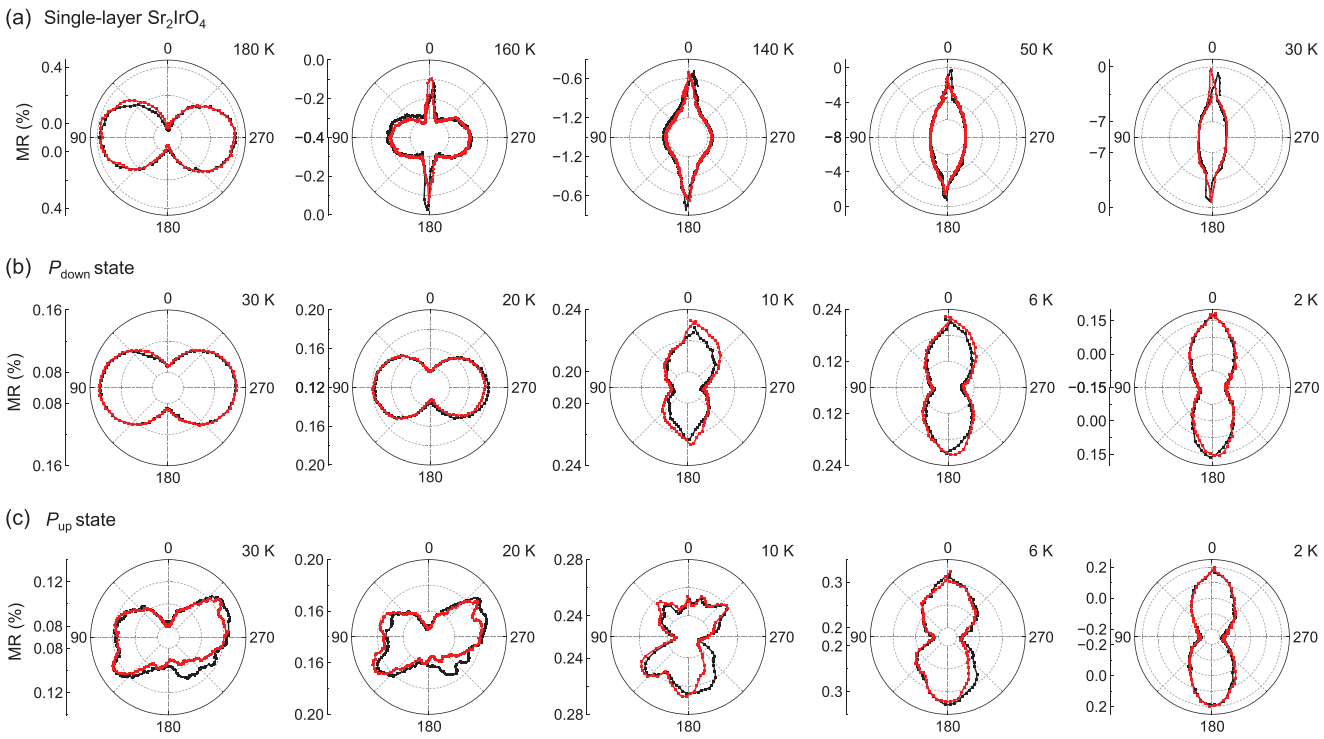

Figure 4. Polar plots of out-of-plane AMR with H field of 5 T at various temperatures. a) Single-layer Sr_2IrO_4. b) P_{down} and c) P_{up} state of PZT/Sr_2IrO_4. The red (black) curves represent the upward (downward) sweep of φ.

Figure 4a shows the polar plot of MR versus φ for single-layer Sr_2IrO_4 at 5 T. At 180 K, the sample resistance can be described by the coherent rotation model[54] as $R_{\square} = R_{avg} + \Delta R\cos[2(\varphi + \varphi_0)]$, with $R_{avg} = \frac{1}{2}[R(0°) + R(90°)]$ and $\Delta R = \frac{1}{2}[R(0°) - R(90°)]$. The second term gives the out-of-plane AMR resistance: $R_{AMR} = \Delta R\cos[2(\varphi + \varphi_0)]$. The MR is positive and R_{AMR} peaks at $\varphi = 90°$ ($\varphi_0 = -90°$), showing that the in-plane MR is larger than the out-of-plane MR. Given that the positive MR originates from the magnetoelastic effect, this is understandable as the in-plane magnetic field can modify the oxygen octahedral rotation. At 160 K, the MR transitions from positive to negative, and an additional component with 90° phase shift emerges. This negative MR is associated with the change in net magnetic moment. Its angular dependence deviates from the $\cos[2(\varphi + \varphi_0)]$ behavior, reflecting the enhanced contribution of MCA. This phase-shifted component becomes dominant at low temperatures and exhibits clear hysteresis along the [001] and [00$\bar{1}$] directions, which can be attributed to the spin-flop transition in out-of-plane magnetic field. Similar temperature evolution of R_{AMR} has previously been observed in Sr_2IrO_4 thin films.[7,18]

Figure 4b shows the angular dependence of MR for the heterostructure in the P_{down} state. The MR also shows a phase shift from $\varphi_0 = -90°$ at high temperatures (20 K and 30 K) to $\varphi_0 = 0°$ at low temperatures (2–10 K). The sharp switching hysteresis in the out-of-plane MR becomes negligibly small in the PZT/Sr_2IrO_4 heterostructure, further supporting that the ferroelectric layer has modified the magnetic state in Sr_2IrO_4. For the P_{up} state (Figure 4c), the low temperature AMR exhibits qualitatively similar angular dependence as those in the P_{down} state, with slightly larger positive MR. At high temperatures (10–30 K), however, despite the consistent peak and valley positions of MR, the angular dependence clearly deviates from the sinusoidal dependence.

Such deviations are clearly illustrated in the R_{AMR} versus φ plots. Above 10 K, the angular dependence of R_{AMR} follows the sinusoidal behavior in the P_{down} state (**Figure** 5a) but exhibits multi-level resistance pinning in the P_{up} state (Figure 5b). At 30 K, in addition to the regions following the $\cos(2\varphi)$ dependence, R_{AMR} in the P_{up} state shows clear pinning behavior to two distinct resistance states along certain crystallin orientations, *i.e.*, pinning at 1.35 Ω in the angular range of [45°, 90°] and [225°, 270°] and pinning at −1.35 Ω in the angular range of [135°, 180°]. Similarly, R_{AMR} at 20 K exhibits multi-level resistance pinning behavior at 0.8 Ω in the field range of [45°, 90°] and [225°, 270°] and pinning at -0.8 Ω in the field range of [135°, 180°]. Similar sharp switching between pinned resistance states has previously been observed in the planar Hall resistance in nanostructured $La_{0.67}Sr_{0.33}MnO_3$ thin films,[55] which has been attributed to enhanced MCA induced magnetization pinning. The pinned resistance levels suggest magnetization pinning along [101], [10$\bar{1}$], and [$\bar{1}$0$\bar{1}$] directions, making <101> the magnetic easy axes. The missing resistance pinning along [$\bar{1}$01] may be due to slight misalignment of the sample plane with respect to the magnetic field.

The fact that such resistance pinning has only been observed in the P_{up} state clearly points to the modulation of MCA via ferroelectric polarization. The ferroelectric field effect modulation of AMR resistance has previously been observed in (La,Sr)MnO_3,[28,29,31] which has been attributed to the modulation

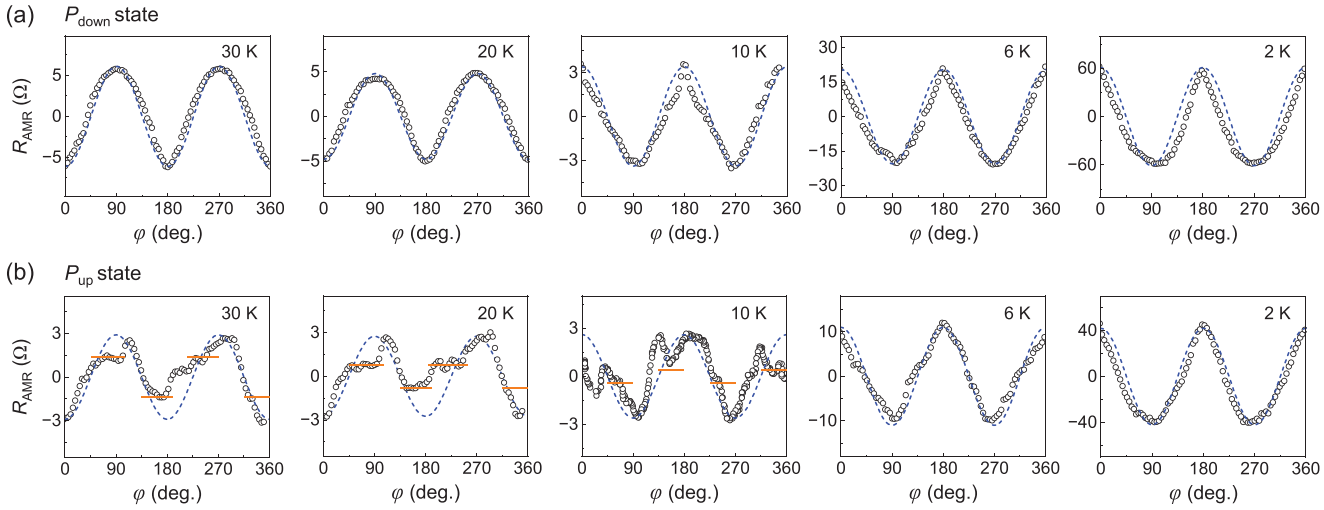

Figure 5. Out-of-plane angular dependence of R_{AMR} with H field of 5 T at various temperatures. a) P_{down} state and b) P_{up} state of PZT/Sr_2IrO_4. The red (black) curves represent the upward (downward) sweep of φ.

of the relative occupation of *d*-orbitals.[30,31] At 10 K, R_{AMR} for the P_{up} state also exhibits a 90° phase shift, similar to that of the P_{down} state. Clear fluctuation occurs in the resistance pinning angles, possibly affected by the competition between the magnetoelastic effect (positive MR) and the induced magnetization (negative MR). As we further cool down the sample, R_{AMR} still exhibits clear kinks, e.g., at $\varphi = 45°$ and 135° at 6 K, which eventually becomes overwhelmed by the substantially enhanced negative MR at 2 K. As this coincides with the temperature range where the sample exhibits pronounced negative MR and possible incipient ferromagnetism, a plausible scenario for the vanishing resistance pinning is the Zeeman energy, which scales with magnetization, is sufficient to overcome the MCA and modifies magnetic energy landscape.[34,55]

3. Conclusion

In summary, we demonstrate nonvolatile ferroelectric field effect control of magenetotransport properties in the epitaxial PZT/Sr_2IrO_4 heterostructure. The presence of PZT drives ultrathin Sr_2IrO_4 to the 2D metallic limit, which has been attributed to the modified lattice distortion due to interfacial atomic coupling. The in-plane MR of the heterostructure shows positive MR at low fields, followed by negative MR at high fields, opposite to the field dependence of single-layer Sr_2IrO_4. The distinct temperature and magnetic field dependences of MR and the absence of spin-flip transition induced MR hysteresis suggests possible emergence of incipient ferromagnetism in the metallic state of Sr_2IrO_4 with the transition temperature close to 6 K. While the out-of-plane AMR in both polarization states shows sinusoidal angular dependence with a temperature-driven 90° phase shift, multi-level resistance pinning emerges in the P_{up} state, revealing the polarization doping induced tuning of magnetic anisotropy. Our findings provide new insights into the intricate interplay of electronic, magnetic, and structural states in Sr_2IrO_4, opening new avenues for exploring correlated phenomena and voltage-controlled functionalities in 5*d*-based Mott insulators.

4. Experimental Section

Sr_2IrO_4 thin films and PZT/Sr_2IrO_4 heterostructures were deposited on (001) LSAT substrates using off-axis radio-frequency magnetron sputtering. The Sr_2IrO_4 layer was grown at 750 °C with 50 mTorr process gas (Ar:O_2 = 16:1). The PZT layer was deposited at 500 °C with 180 mTorr process gas (Ar:O_2 = 32:1). After PZT deposition, the sample was cooled down to room temperature in an O_2 atmosphere. For the field effect study, PZT/Sr_2IrO_4 heterostructures were deposited on LSAT substrates prepatterned into Hall bar geometry, followed by lithography and Au electrode deposition. Detailed information for device fabrication can be found in Ref. [20].

XRD measurements were carried out using a Rigaku SmartLab Diffractometer with a Cu Kα radiation source (λ = 1.5406 Å). Transport measurements were performed using a Quantum Design Physical Property Measurement System with either Keithley 2400 SourceMeters or Stanford Research Systems SR830 lock-in amplifiers. The sample resistance was characterized using a wide range of current densities varying from 0.19–53.85 μA μm^{-2} to rule out Jule heating and current-induced metal-insulator transition. The resistance of both single-layer and heterostructure samples does not show apparent dependence on the current density (Figure S3, Supporting Information). No Joule heating effect was observed at low temperature. AFM and PFM studies were conducted using a Bruker Multimode 8 AFM.

Supporting Information

Supporting Information is available from the Wiley Online Library or from the author.

Acknowledgements

The authors would like to thank Jia Wang and Tianlin Li for valuable discussions and Xin Li for technical support. This work was supported by NSF EPSCoR RII Track-1: Emergent Quantum Materials and Technologies (EQUATE), Award No. OIA-2044049, the UNL Grand Challenges catalyst award entitled Quantum Approaches addressing Global Threats, and the Nebraska Center for Energy Sciences Research. The research was conducted, in part, at the Nebraska Nanoscale Facility: National Nanotechnology Coordinated Infrastructure and the Nebraska Center for Materials and Nanoscience, supported by the National Science Foundation under Award No. ECCS: 2025298, and the Nebraska Research Initiative.

Conflict of Interest

The authors declare no conflict of interest.

Data Availability Statement

The data that support the findings of this study are available from the corresponding author upon reasonable request.

Keywords

2D transport, anisotropic magnetoresistance, ferroelectric field effect, incipient ferromagnetism, Mott insulator, Sr_2IrO_4

Received: December 31, 2024
Revised: April 8, 2025
Published online: May 12, 2025

[1] G. Cao, P. Schlottmann, *Rep. Prog. Phys.* **2018**, *81*, 042502.
[2] S. J. Moon, H. Jin, K. W. Kim, W. S. Choi, Y. S. Lee, J. Yu, G. Cao, A. Sumi, H. Funakubo, C. Bernhard, T. W. Noh, *Phys. Rev. Lett.* **2008**, *101*, 226402.
[3] B. J. Kim, H. Jin, S. J. Moon, J.-Y. Kim, B.-G. Park, C. S. Leem, J. Yu, T. W. Noh, C. Kim, S.-J. Oh, J.-H. Park, V. Durairaj, G. Cao, E. Rotenberg, *Phys. Rev. Lett.* **2008**, *101*, 076402.
[4] G. Cao, J. Terzic, H. D. Zhao, H. Zheng, L. E. De Long, P. S. Riseborough, *Phys. Rev. Lett.* **2018**, *120*, 017201.
[5] J. Nichols, J. Terzic, E. G. Bittle, O. B. Korneta, L. E. De Long, J. W. Brill, G. Cao, S. S. A. Seo, *Appl. Phys. Lett.* **2013**, *102*, 141908.
[6] N. Hu, Y. K. Weng, K. Chen, B. You, Y. Liu, Y. T. Chang, R. Xiong, S. Dong, C. L. Lu, *Mater. Today Phys.* **2022**, *27*, 100809.
[7] L. Miao, H. Xu, Z. Q. Mao, *Phys. Rev. B* **2014**, *89*, 035109.
[8] S. Shrestha, M. Krautloher, M. Zhu, J. Kim, J. Hwang, J. Kim, J. W. Kim, B. Keimer, A. Seo, *Phys. Rev. B.* **2022**, *105*, L100404.
[9] C. H. Ahn, A. Bhattacharya, M. Di Ventra, J. N. Eckstein, C. D. Frisbie, M. E. Gershenson, A. M. Goldman, I. H. Inoue, J. Mannhart, A. J. Millis, A. F. Morpurgo, D. Natelson, J.-M. Triscone, *Rev. Mod. Phys.* **2006**, *78*, 1185.
[10] F. Wang, T. Senthil, *Phys. Rev. Lett.* **2011**, *106*, 136402.
[11] O. B. Korneta, T. Qi, S. Chikara, S. Parkin, L. E. De Long, P. Schlottmann, G. Cao, *Phys. Rev. B* **2010**, *82*, 115117.
[12] M. Ge, T. F. Qi, O. B. Korneta, D. E. De Long, P. Schlottmann, W. P. Crummett, G. Cao, *Phys. Rev. B* **2011**, *84*, 100402.
[13] T. F. Qi, O. B. Korneta, L. Li, K. Butrouna, V. S. Cao, X. Wan, P. Schlottmann, R. K. Kaul, G. Cao, *Phys. Rev. B* **2012**, *86*, 125105.
[14] S. Calder, G. X. Cao, M. D. Lumsden, J. W. Kim, Z. Gai, B. C. Sales, D. Mandrus, A. D. Christianson, *Phys. Rev. B* **2012**, *86*, 220403.
[15] Y. Cao, Q. Wang, J. A. Waugh, T. J. Reber, H. Li, X. Zhou, S. Parham, S.-R. Park, N. C. Plumb, E. Rotenberg, A. Bostwick, J. D. Denlinger, T. Qi, M. A. Hermele, G. Cao, D. S. Dessau, *Nat. Commun.* **2016**, *7*, 11367.
[16] F. Wen, X. Liu, Q. Zhang, M. Kareev, B. Pal, Y. Cao, J. W. Freeland, A. T. N'Diaye, P. Shafer, E. Arenholz, L. Gu, J. Chakhalian, *New J. Phys.* **2019**, *21*, 103009.
[17] J. Ravichandran, C. R. Serrao, D. K. Efetov, D. Yi, Y. S. Oh, S. W. Cheong, R. Ramesh, P. Kim, *J. Phys.: Condens. Matter* **2016**, *28*, 505304.
[18] C. Lu, S. Dong, A. Quindeau, D. Preziosi, N. Hu, M. Alexe, *Phys. Rev. B* **2015**, *91*, 104401.
[19] M. A. Hope, K. J. Griffith, B. Cui, F. Gao, S. E. Dutton, S. S. P. Parkin, C. P. Grey, *J. Am. Chem. Soc.* **2018**, *140*, 16685.
[20] Y. Hao, X. Chen, L. Zhang, M.-G. Han, W. Wang, Y.-W. Fang, H. Chen, Y. Zhu, X. Hong, *Nat. Commun.* **2023**, *14*, 8247.
[21] M. S. Marshall, A. Malashevich, A. S. Disa, M.-G. Han, H. Chen, Y. Zhu, S. Ismail-Beigi, F. J. Walker, C. H. Ahn, *Phys. Rev. Appl.* **2014**, *2*, 051001.
[22] X. Hong, A. Posadas, C. H. Ahn, *Appl. Phys. Lett.* **2005**, *86*, 142501.
[23] T. Yajima, T. Nishimura, T. Tanaka, K. Uchida, A. Toriumi, *Adv. Electron. Mater.* **2020**, *6*, 1901356.
[24] C. H. Ahn, S. Gariglio, P. Paruch, T. Tybell, L. Antognazza, J. M. Triscone, *Science* **1999**, *284*, 1152.
[25] A. Crassous, R. Bernard, S. Fusil, K. Bouzehouane, J. Briatico, M. Bibes, A. Barthelemy, J. E. Villegas, *J. Appl. Phys.* **2013**, *113*, 024910.
[26] H. J. A. Molegraaf, J. Hoffman, C. A. F. Vaz, S. Gariglio, D. van der Marel, C. H. Ahn, J. M. Triscone, *Adv. Mater.* **2009**, *21*, 3470.
[27] C. A. F. Vaz, J. Hoffman, Y. Segal, J. W. Reiner, R. D. Grober, Z. Zhang, C. H. Ahn, F. J. Walker, *Phys. Rev. Lett.* **2010**, *104*, 127202.
[28] X. Hong, J. B. Yau, J. D. Hoffman, C. H. Ahn, Y. Bason, L. Klein, *Phys. Rev. B* **2006**, *74*, 174406.
[29] D. Preziosi, I. Fina, E. Pippel, D. Hesse, X. Marti, F. Bern, M. Ziese, M. Alexe, *Phys. Rev. B* **2014**, *90*, 125155.
[30] D. Preziosi, M. Alexe, D. Hesse, M. Salluzzo, *Phys. Rev. Lett.* **2015**, *115*, 157401.
[31] A. Rajapitamahuni, L. L. Tao, Y. Hao, J. Song, X. Xu, E. Y. Tsymbal, X. Hong, *Phys. Rev. Mater.* **2019**, *3*, 021401.
[32] S. Q. A. Shah, M. Annaorazov, G. Rimal, J. Wang, M. F. Borunda, J. Tang, A. J. Yost, *ACS Appl. Mater. Interfaces* **2023**, *15*, 10141.
[33] C. A. F. Vaz, Y. J. Shin, M. Bibes, K. M. Rabe, F. J. Walker, C. H. Ahn, *Appl. Phys. Rev.* **2021**, *8*, 041308.
[34] Y. F. Hao, T. L. Li, X. Hong, *Chem. Commun.* **2025**, *61*, 4924.
[35] H. Yamada, M. Marinova, P. Altuntas, A. Crassous, L. Begon-Lours, S. Fusil, E. Jacquet, V. Garcia, K. Bouzehouane, A. Gloter, et al., *Sci. Rep.* **2013**, *3*, 2834.
[36] Y. W. Yin, J. D. Burton, Y.-M. Kim, A. Y. Borisevich, S. J. Pennycook, S. M. Yang, T. W. Noh, A. Gruverman, X. G. Li, E. Y. Tsymbal, Q.i Li, *Nat. Mater.* **2013**, *12*, 397.
[37] Z. Wen, D. Wu, *Adv. Mater.* **2020**, *32*, 1904123.
[38] Y. Zhang, Y. Hao, L. Zhang, K. Wang, X. Hong, *Appl. Phys. Lett.* **2024**, *125*, 102904.
[39] V. Garcia, S. Fusil, K. Bouzehouane, S. Enouz-Vedrenne, N. D. Mathur, A. Barthélémy, M. Bibes, *Nature* **2009**, *460*, 81.
[40] Y. Klein, I. Terasaki, *J. Electron. Mater.* **2009**, *38*, 1331.
[41] L. Zhang, X. G. Chen, H. J. Gardner, M. A. Koten, J. E. Shield, X. Hong, *Appl. Phys. Lett.* **2015**, *107*, 152906.
[42] C. Lu, A. Quindeau, H. Deniz, D. Preziosi, D. Hesse, M. Alexe, *Appl. Phys. Lett.* **2014**, *105*, 082407.
[43] B. I. Shklovskii, A. L. Efros, in *Electronic Properties of Doped Semiconductors*, Springer, Berlin, Heidelberg **1984**, p. 202.
[44] X. Hong, K. Zou, B. Wang, S. H. Cheng, J. Zhu, *Phys. Rev. Lett.* **2012**, *108*, 226602.
[45] P. A. Lee, T. V. Ramakrishnan, *Rev. Mod. Phys.* **1985**, *57*, 287.
[46] D. J. Bishop, R. C. Dynes, D. C. Tsui, *Phys. Rev. B.* **1982**, *26*, 773.
[47] E. H. Hwang, S. D. Sarma, *Phys. Rev. B.* **2008**, *77*, 115449.
[48] G. A. Rossetti, *British Ceramic Transactions* **2004**, *103*, 83.
[49] C. Lu, B. Gao, H. Wang, W. Wang, S. Yuan, S. Dong, J.-M. Liu, *Adv. Funct. Mater.* **2018**, *28*, 1706589.
[50] G. Cao, J. Bolivar, S. McCall, J. E. Crow, R. P. Guertin, *Phys. Rev. B.* **1998**, *57*, R11039.

[51] F. Ye, S. Chi, B. C. Chakoumakos, J. A. Fernandez-Baca, T. Qi, G. Cao, *Phys. Rev. B.* **2013**, *87*, 140406.
[52] C. Zener, *Phys. Rev.* **1951**, *82*, 403.
[53] B. J. Kim, H. Ohsumi, T. Komesu, S. Sakai, T. Morita, H. Takagi, T. Arima, *Science* **2009**, *323*, 1329.
[54] T. Li, L. Zhang, X. Hong, *Journal of Vacuum Science & Technology A.* **2022**, *40*, 010807.
[55] A. K. Rajapitamahuni, L. Zhang, M. A. Koten, V. R. Singh, J. D. Burton, E. Y. Tsymbal, J. E. Shield, X. Hong, *Phys. Rev. Lett.* **2016**, *116*, 187201.